

Earthquake-induced impact of base-isolated buildings: theory, numerical modeling, and design solutions

Ching-Ching Yu¹, Andrew S. Whittaker¹, Benjamin D. Kosbab², and Payman Khalili Tehrani³

Corresponding Author Mail ID - cyu23@buffalo.edu

¹Department of Civil, Structural, and Environmental Engineering, University at Buffalo, Buffalo, NY 14228

²Simpson Gumpertz & Heger, 600 Galleria Parkway, Suite 1670, Atlanta, GA 30339

³SC Solutions, 1261 Oakmead Parkway, Sunnyvale, CA 94085

Earthquake shaking more intense than that used to size the horizontal clearance between a base-isolated building and near-rigid perimeter moat wall will result in hard impact, producing high-frequency, high-amplitude acceleration response in the structure and supported equipment. This paper provides a design solution for the damaging effects of hard impact by installing a compliant engineered element in the load path between the base-isolated building and the moat wall, resulting in soft impact and a much smaller acceleration response. The engineered element assumed herein is commercial-off-the-shelf marine fender with mechanical properties determined by physical testing. The attachment of a flexible engineered element, with well-defined stiffness and damping, to a near-rigid moat wall, simplifies the numerical modeling of the building-moat wall system and eliminates the need to bound the lateral stiffness of the wall for impact calculations. The simple model of the engineered element can be implemented in commercial finite element codes. Theory is developed for two-sided impact of a single-degree-of-freedom oscillator. Analytical solutions are derived for the shifted first-mode frequency of the impacted oscillator and for its free-vibration response. The shifted first-mode frequency is a function of the composite lateral stiffness of the isolator-engineered element assembly and its earthquake-induced displacement. Local peaks in the spectral response of the impacted oscillator form at odd integer multiples of the shifted first-mode frequency. The analytical solutions can be used to verify, in part, the numerical model used for impact analysis.

Keywords

Base isolation, impact, design solutions, engineered restraints, theory, verification

NOVELTY

- A compliant engineered displacement restraint installed between a base-isolated building and a perimeter moat wall can mitigate the high-amplitude, high-frequency accelerations generated by impact
- Theory is developed to identify the shifted first-mode frequency and those of the local peaks in the acceleration response spectrum of a base-isolated building undergoing two-sided impact, which enables partial verification of a numerical model.
- The stiffness and damping properties of an engineered restraint can be selected to strike a balance between isolation-system displacement and building acceleration response in the event of impact.

Introduction

Seismic base isolation can substantially mitigate the effects of earthquake ground shaking on buildings, bridges, and infrastructure, but reductions in accelerations are accompanied by an increase in displacements across the isolation plane. An isolated building is shown in Figure 1¹, which is surrounded by a perimeter *moat wall*. The horizontal movement of the isolated building is not restricted until the ground shaking is sufficiently intense to close the gap (or clearance) between it and the wall. Impact on a near-rigid moat wall (i.e., a *hard* restraint resulting in *hard* impact) will generate high-frequency, high-amplitude shaking in the isolated building²⁻⁵.

This is the author manuscript accepted for publication and has undergone full peer review but has not been through the copyediting, typesetting, pagination and proofreading process, which may lead to differences between this version and the [Version of Record](#). Please cite this article as [doi: 10.1002/eqe.3824](https://doi.org/10.1002/eqe.3824).

This article is protected by copyright. All rights reserved.

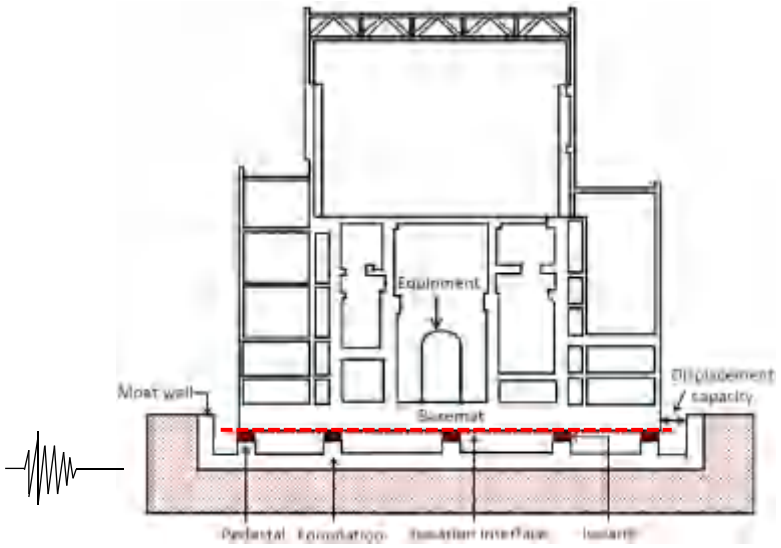


Figure 1. Base isolated building¹

Impact is unlikely to occur in the lifetime of an isolated structure in the United States because of the rules implemented in codes and standards (e.g., ASCE/SEI 7-22⁶), setting a minimum horizontal clearance between the building and adjacent structure (e.g., a moat wall) based on isolation-system displacements calculated for shaking with a very small probability (e.g., 2%) of exceedance in 50 years. Also, a minimum horizontal clearance to avoid impact of the base-isolated building on a perimeter moat wall, at a user-specified annual frequency of exceedance, can be easily established⁷. However, the response of an isolated building to earthquake shaking more intense than that used to size the horizontal clearance may need to be analyzed in support of risk calculations. Assessing the results of hard impact is challenging because the computed acceleration response in the building is extremely sensitive to the assumed lateral stiffness of the restraint, which will generally be constructed of reinforced concrete and backed by compacted soil.

Wolf and Skrikerud published a seminal article⁸ on earthquake-induced impact of buildings. Sample results for one-sided hard impact from that study are reproduced in Figure 2 for a 1-Hz oscillator subjected to 1-g broadband earthquake inputs for two boundary conditions: 1) no impact, and 2) impact on a near-rigid restraint with zero gap. For the impact case, the spectral accelerations exceed 20 g at frequencies greater than 10 Hz, which would challenge the design of any building framing system and equipment. Wolf and Skrikerud⁸ developed equations for the shifted first mode frequency (= 2 Hz in Figure 2) and the local peaks (black open-headed arrows in Figure 2) in the spectrum at higher frequencies.

High-frequency, high-amplitude earthquake response of a base isolated building associated with hard impact will be mitigated if a compliant engineered *restraint* is introduced between the basemat and the moat wall: *soft impact*. Analysis of soft impact is straightforward, avoids the judgments required for hard impact simulations, and can be accomplished using simple numerical models available in finite element software.

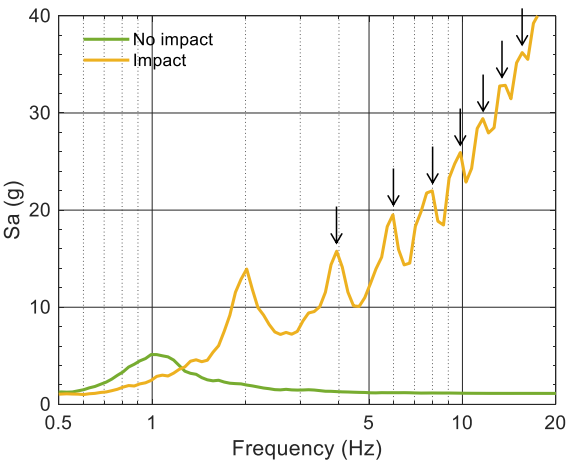


Figure 2. Five percent-damped response spectra for a 1-Hz oscillator, with details per Appendix B.

Section 0 of the paper presents theory, building on Wolf and Skrikerud⁸, to enable verification of numerical models for analysis of two-sided impact with *soft* or *hard* restraints. Section 0 describes the engineering of a compliant displacement restraint and numerical modeling of the corresponding isolated building-restraint-wall system. The analytical and numerical tools presented in Sections 0 and 3, respectively, are agnostic to the building function, chosen isolation system, clearance, restraint type and mechanical properties, and performance objectives. Section 0 provides design solutions for impact of buildings isolated on bilinear bearings, revisits *hard* impact, and illustrates the merits of soft versus hard impact. Section 0 presents closing remarks that are relevant to design practice.

Two appendices follow the body of this paper and provide background information relevant to this article. Appendix A summarizes published models for *general* impact analysis and introduces studies on impact analysis of base-isolated buildings. The literature review is not presented in the body of this paper because the analysis approaches presented in prior studies are substantially different from that pursued here. Appendix B reviews Wolf and Skrikerud⁸, corrects a presented analytical solution, and generates numerical solutions for one-sided impact to confirm results and trends presented in that paper.

Analytical solutions for two-sided impact

An analytical approach based on Timoshenko (1937)⁹ and Timoshenko et al. (1974)¹⁰ is developed here to identify the frequency and free-vibration response of a single-degree-of-freedom (SDF) oscillator, subjected to two-sided impact, as shown in Figure 3. The oscillator is characterized by a mass, m , and a linear spring with stiffness, k . To address impact, two *impact* springs with stiffness k_e are attached to the rigid boundary. The stiffness k_e can be either linear or nonlinear. The at-rest clearance (or gap) between the oscillator and the impact springs is e . The oscillator displacement relative to the ground is x . Per Figure 3b, the relationship between the spring force, $F(x)$, on the oscillator and x is nonlinear. The $F(x)$ - x relationship is a function of k , k_e , and e . If $|x| \leq e$, the oscillator is not in contact with the impact springs and $F(x)$ is proportional to k . If $|x| > e$, the oscillator is attached to one of the impact springs and the increment of $F(x)$ is proportional to $k+k_e$. No damping force is considered. The parameters defined in Figure 3 (i.e., m , k , k_e , and e) are consistent with those used in Wolf and Skrikerud (1980)⁸: see Appendix B. Different from Wolf and Skrikerud⁸, the approach presented here can be used for nonlinear k_e .

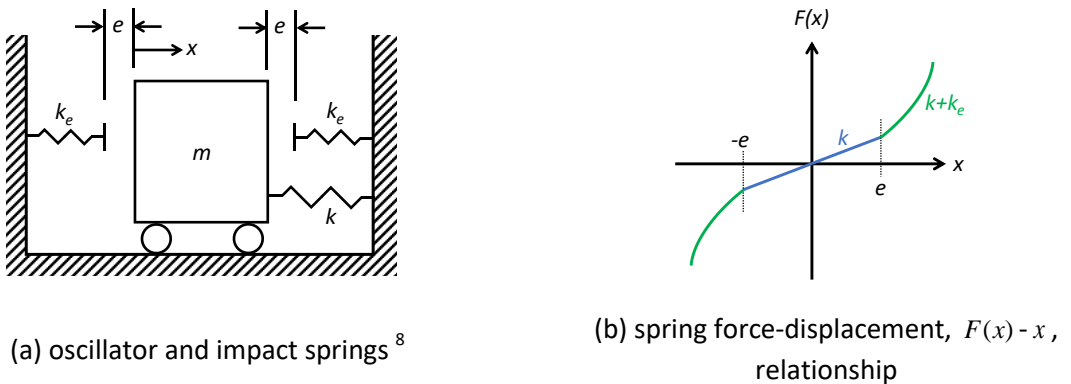


Figure 3. Oscillator subjected to two-sided impact

The initial condition for the free-vibration response of the oscillator is a positive displacement \bar{x} . If $\bar{x} \leq e$, the angular frequency of the oscillator is $\omega = \sqrt{k/m}$. If $\bar{x} > e$, an impact spring is engaged and the angular frequency is $\bar{\omega}$, which is higher than ω due to the greater stiffness: $k+k_e$. The equation of motion for the oscillator, composed of the inertial force, $m\ddot{x}$, and the spring force, $F(x)$, is used to derive analytical solutions for $\bar{\omega}$ and x .

Per Figure 3b, the $F(x)-x$ relationship is symmetrical about the origin, namely, an odd function. Given \bar{x} , the spring force F can be approximated using a polynomial function of x with odd powers. A 3rd-degree polynomial function is assumed here:

$$\bar{F} = c_1x + c_3x^3 \quad (1)$$

where \bar{F} is the approximate value for F for $-\bar{x} \leq x \leq \bar{x}$; c_1 and c_3 are positive coefficients generated per regression analysis. A change in \bar{x} will affect the values of c_1 and c_3 .

The equation of motion for the oscillator is the sum of the inertial force, $m\ddot{x}$, and the approximate spring force, Γ :

$$m\ddot{x} + c_3x^3 = 0 \quad (2)$$

Equation (2) can be solved for the angular frequency $\bar{\omega}$ and the free-vibration response x using a procedure presented on pages 129 to 134 of Timoshenko⁹ (or pages 168 to 175 in Timoshenko, et al.¹⁰):

$$\bar{\omega} = \sqrt{\frac{c_1}{m} + \frac{3c_3\bar{x}^2}{4m}} \quad (3)$$

$$x = (\bar{x} - \frac{c_3\bar{x}^3}{32\bar{\omega}^2 m}) \cos \bar{\omega}t + \frac{c_3\bar{x}^3}{32\bar{\omega}^2 m} \cos 3\bar{\omega}t \quad (4)$$

where c_1/m , c_3/m , and $\bar{\omega}$ are termed p^2 , α , and p_1 , respectively, in the Timoshenko textbooks (see Eqs. (e) and (56) in Timoshenko⁹, and Eqs. (2.15) and (2.16) in Timoshenko, et al.¹⁰).

Equations (3) and (4) are the first-order approximations for $\bar{\omega}$ and x , respectively. The free-vibration response x per Eq. (4) is the sum of two sinusoids at $\bar{\omega}$ and $3\bar{\omega}$. (The third-order approximation for x is the sum of four sinusoids at $\bar{\omega}$, $3\bar{\omega}$, $5\bar{\omega}$, and $7\bar{\omega}$: see Eq. (2.20) on page 174 in Timoshenko, et al.¹⁰). The number of sinusoids included in the solution for x increases with the increasing order of the approximation. The exact solution for x is an infinite sum of sinusoids with angular frequencies of $\bar{\omega}$ and odd-number multiples (i.e., 3, 5, 7, 9, 11, etc.) of $\bar{\omega}$. Accordingly, the response spectrum for an oscillator generated by two-sided impact will peak locally at $\bar{\omega}$ and odd-number multiples of $\bar{\omega}$: different from the integer multiples for one-sided impact shown in Figure 2 and described in Appendix B. These theoretical outcomes are used in Section 3 to verify the results of numerical analysis. For the case of no impact, $\bar{x} \leq e$, $c_1 = k$, and $c_3 = 0$. The solution for $\bar{\omega}$ per Eq. (3) is $\sqrt{k/m}$, namely $\bar{\omega} = \omega$, and Eq. (4) collapses to $x = \bar{x} \cos \omega t$.

Engineering a displacement restraint

Introduction

A compliant engineered displacement restraint can be used to substantially mitigate the damaging effects of *hard* impact, namely, high-amplitude, high-frequency acceleration response per Figure 2. The process to implement a compliant restraint is introduced using a building with plan dimensions of 25 m by 25 m, a height of 32 m, and a mass, including the basemat, of 9,000 tonnes. A 2D horizontal seismic isolation system is installed below the basemat and above the foundation: see Figure 1. For this example, the isolation system is composed of low damping natural rubber (LDR) bearings, assumed to be linear-viscoelastic, with a period of 2 seconds. (Bilinear isolation systems are addressed in Section 0.) The corresponding horizontal stiffness of the isolation system, k , is 88 kN/mm.

1.2 Mechanical behavior of an engineered displacement restraint

The engineered displacement restraint considered herein is a heavy-duty, commercial-off-the-shelf, marine fender. The marine fender is attached to the moat wall, which is assumed to be rigid. (The selection of a displacement restraint, either commercially available or a custom design, and its attachment to the moat wall would be project specific, which is beyond the scope of this paper. A

near-rigid wall could be constructed by buttressing it from the foundation.) If the wall is near-rigid, the flexibility of the restraint-wall system is that of the fender only, enabling its accurate modeling and avoiding the need to bound the lateral stiffness of wall-compacted soil assembly. The chosen fender is square in cross section, with a central hole, and a length parallel to the perimeter of the basemat of 25 m: see Figure 4a, which is adapted from a marine fender catalog (ShibataFenderTeam 2022¹¹). The fender has a width, w , of 250 mm and the diameter of the central hole, d , is 125 mm. The maximum deformation of interest for design of marine fenders is the diameter of the central hole, for which the manufacturer provides test data. Here, and for completeness, the maximum fender deformation considered for analysis is assumed to be greater than d . The rubber block of Figure 4b is assumed to represent the fender after the central hole has been closed.

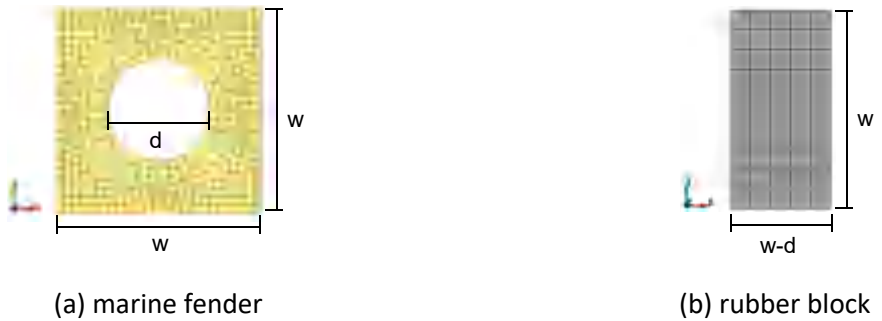


Figure 4. Numerical models for the marine fender

Force-displacement test data are available for the fender of Figure 4a for a maximum displacement of $d = 125$ mm. To confirm the test results, the compression stiffness of the marine fender was computed using LS-DYNA¹². Figure 4 identifies the solid elements used to model the marine fender and rubber block, which are assigned the material card *MAT_MOONEY-RIVLIN_RUBBER and mechanical properties consistent with International Rubber Hardness Degree = 70. Figure 5a presents the force-displacement relationship in the x direction, presented for the 25-m long fender of Figure 4a. The stiffness is linear, equal to 86 kN/mm ($= k_{el}$), consistent with the secant stiffness computed using the manufacturer's data. To estimate the compression stiffness of the fender for displacements greater than d , the solid rectangular rubber block of Figure 4b was analyzed: width = $w - d = 0.5w$ and height = w . Figure 5b presents the force-displacement relationship for a 25-m long rectangular rubber block, which is assumed to be bi-linear and characterized by k_{e2} ($= 358$ kN/mm) and k_{e3} ($= 700$ kN/mm). (For design and construction, the mechanical properties of displacement restraints, including force-displacement relationships, should be determined by physical testing and catalogued.)

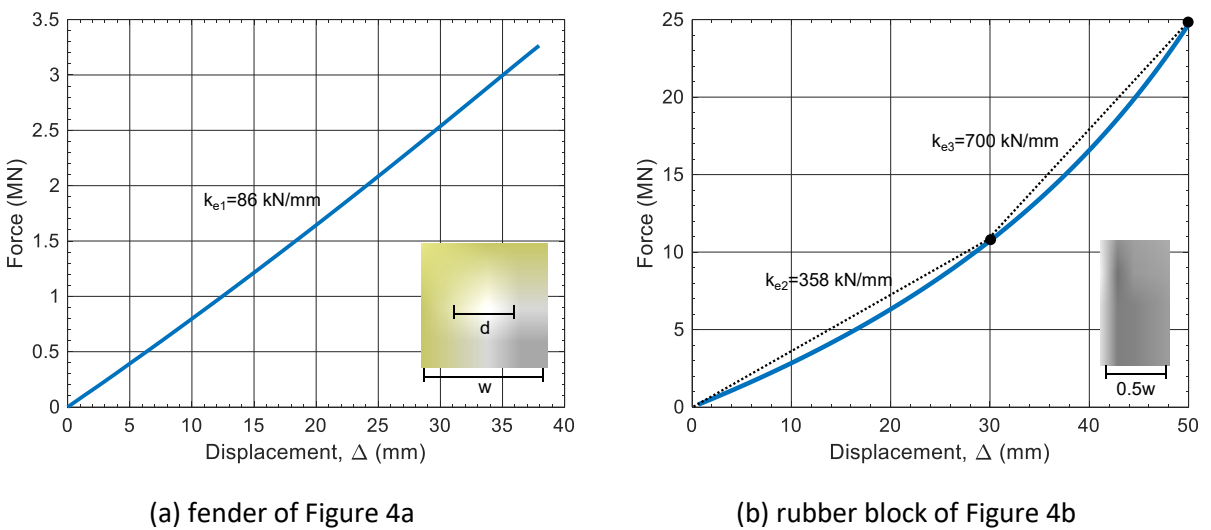


Figure 5. Force-displacement relationships for a fender, $w = 250 \text{ mm}$, $d = 125 \text{ mm}$, and length of 25 m

The force-displacement relationship for the fender can be described as trilinear per Figure 6a, with stiffness increasing with displacement, Δ , namely, k_{e1} for $0 < \Delta < d$, k_{e2} for $d \leq \Delta < d + 30 \text{ mm}$, and k_{e3} for $d + 30 \text{ mm} \leq \Delta$. Figure 6b presents the composite force-displacement response, $F(x) - x$, of the isolation system with fenders on both sides of the building, for gap, e , equal to 100 mm and 200 mm. The stiffness associated with the four slopes on either side of the origin in Figure 6b is k , $k + k_{e1}$, $k + k_{e2}$, and $k + k_{e3}$. Changing the gap alters the composite force-displacement relationship. The distance between the edge of the building and the moat wall is $e + w$.

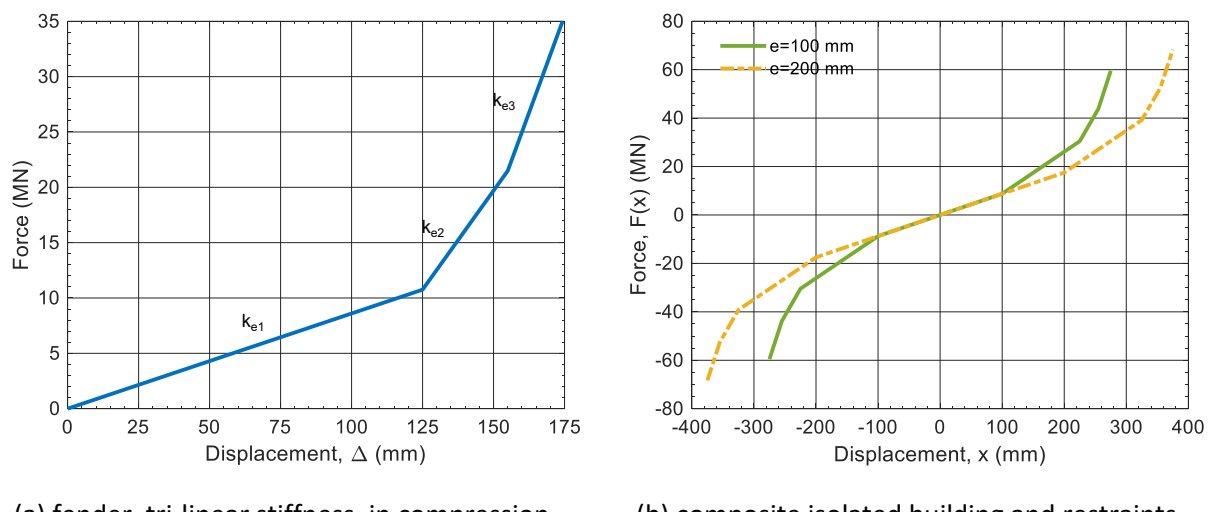


Figure 6. Force-displacement relationships, 2-second isolated building, 25-m long restraints with $w = 250 \text{ mm}$ and $d = 125 \text{ mm}$

The analytical solution for the shifted first modal frequency, $\bar{\omega}$, computed from the composite force-displacement relationship of Figure 6b, and the frequencies of the local peaks at odd multiples of $\bar{\omega}$ in the acceleration response spectrum, enable verification of results of dynamic analysis and provide insight into impact-related responses, as explained below.

Impact analysis of a base-isolated building

Response-history analysis of a single degree of freedom (SDF) model of the isolated building incorporating the engineered displacement restraint of Section 3.2, with $e = 100$ mm, $w = 250$ mm, and $d = 125$ mm, is performed using SAP 2000¹³. The compression stiffness of the restraint is defined in Figure 6a. The force-displacement relationship for the SDF representation of the isolated building is the green solid line in Figure 6b. This combination of isolation system, fender, gap, and input ground motions, as introduced below, enables the generation of earthquake-induced impact responses as different tangent stiffnesses of the fender (i.e., k_{e1} , k_{e2} , and k_{e3}) are engaged.

Figure 7 presents the 5%-damped, geomean, horizontal uniform hazard response spectrum (UHRS) used for response-history analysis: solid yellow line. The peak ground acceleration (PGA) is 1 g. Generated using hazard data published by the United States Geological Survey (USGS)¹⁴, this UHRS could represent 1) 25,000-year earthquake shaking at a soft-rock or stiff-soil site (C/D per ASCE/SEI 7-16) in the Central and Eastern US, and 2) 10,000-year earthquake shaking at a soft rock site (B per ASCE/SEI 7-16) in the Western US. Thirty seed motions were spectrally matched using RSPMatch2005¹⁵ to the target UHRS for frequencies between 0.2 and 50 Hz. The 5%-damped spectral accelerations of the 30 matched motions are shown in grey in Figure 7.

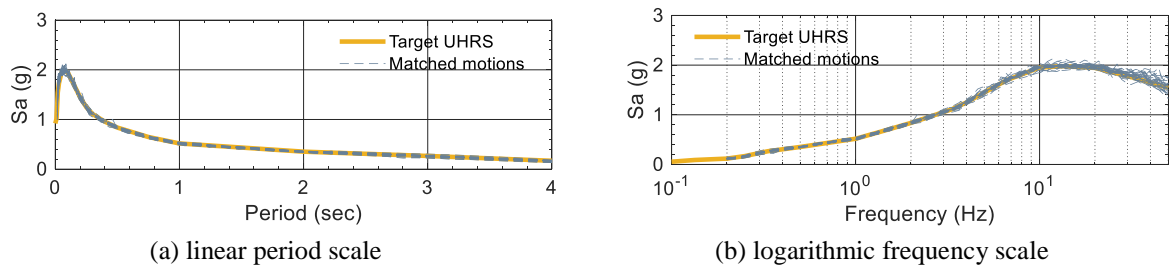


Figure 7. Acceleration response spectra, S_a , for input motions, 5% damping

Figure 8 and Table 1 describe the numerical model used for impact analysis of the base-isolated building. The mass of the building is lumped on the basemat, at the same level as the displacement restraint. The damping ratio for the linear isolation system is assumed to be 5%, modeled using a viscoelastic dashpot with coefficient $c = 2.8$ kN-s/mm. The displacement restraint is modeled using the orange impact elements in Figure 8, each of which includes a spring, k_e , and a dashpot, c_e . Stiffness k_e accommodates the tri-linear stiffness (i.e., k_{e1} , k_{e2} , and k_{e3}) of Figure 6a. For $\Delta > 175$ mm, the tangent stiffness is assumed equal to k_{e3} . Five percent damping is assumed for the restraint and calculated using k_{e1} , namely, $c_e / (2\sqrt{mk_{e1}}) = 5\%$ and $c_e = 2.8$ kN-s/mm. (If $\Delta > 125$ mm, namely, the tangent stiffness is either k_{e2} or k_{e3} (see Figure 6a), the damping ratio is less than 5%.) A gap element, shown as green in Figure 8, is introduced between the building and each impact element. These gap elements are assigned zero stiffness in compression for $\Delta < e$ and in tension for all Δ . For

$\Delta \geq e$ in compression, the elements are *numerically rigid*: the stiffness is 3+ orders of magnitude greater than k_{e3} .

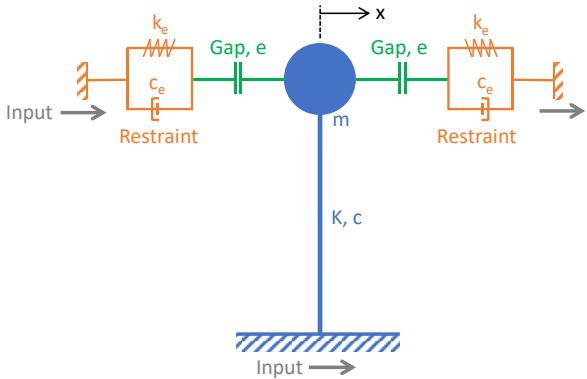


Figure 8. Numerical model for earthquake-induced impact analysis

Table 1. Properties used for seismic analysis of the model shown in Figure 8

Oscillator	m	9×10^3 Tonne
	k	88 kN/mm
	c	2.8 kN-s/mm
Gap width	e	100 mm
Impact element	k_e (see Figure 6a)	$k_{e1} = 86$ kN/mm for 0 to 125 mm $k_{e2} = 358$ kN/mm for 125 to 155 mm $k_{e3} = 700$ kN/mm for 155+ mm
	c_e	2.8 kN-s/mm

Impact analysis outcomes and numerical model verification

Figure 9 presents responses from the dynamic analysis of the model of Figure 8 for one earthquake input in the x direction: (a) displacement of the isolation system, (b) acceleration on the basemat, (c) 5%-damped response spectrum on the basemat, and (d) horizontal force in the opposing restraints (i.e., fenders). Two sets of data are presented in panels (a), (b), and (c): with the restraint described by Figure 6a, and no restraint (i.e., unrestricted displacement of the isolation system). For this input, the restraint reduces the peak displacement from 345 mm to 280 mm. (Both displacements are easily accommodated by modern seismic isolation systems.) The displacement that closes the gap (= 100 mm) is identified using grey dashed lines. There are 12 impacts on each restraint for this input motion, a gap of 100 mm, and the 2-second isolation system. The green dashed lines in Figure 9a identify the displacement that closes the central hole in the restraint (i.e., $e+d=100+125=225$ mm), beyond which there is an increase in the restraint stiffness from k_{e1} to k_{e2} and k_{e3} . Expectedly, the time (=11.5 seconds) of maximum acceleration on the basemat coincides with the maximum displacement in the isolation system, which, for this ground motion input, is associated with stiffness k_{e3} . Figure 9c presents the spectra calculated using the acceleration time series of Figure 9b. The addition of the displacement restraints to the isolation system leads to a reduction in maximum

basemat displacement but an appreciable increase in spectral accelerations, for frequencies between 0.5 and 50 Hz. The peak in the acceleration response spectrum shifts from 0.5 Hz (no restraint, 2-second isolation system) to a higher frequency. Figure 9d presents the horizontal forces in the opposing restraints: the sum of the spring and damping forces in the orange elements of Figure 8.

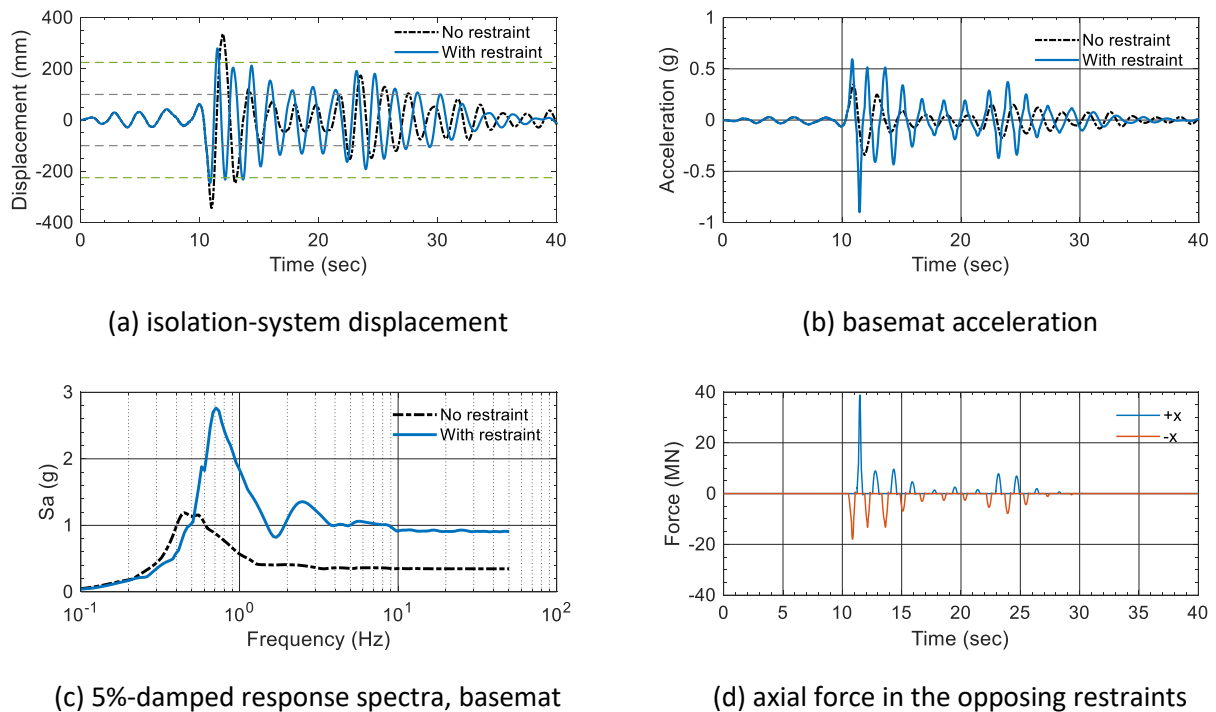


Figure 9. Response-history results, 2-second isolated building, 25-m long restraints with $w = 250$ mm and $d = 125$ mm, and $e = 100$ mm, one matched ground motion, PGA = 1 g

The mean maximum displacement of the basemat of the isolated building for the 30 inputs, without and with the restraint, is 345 mm and 256 mm, respectively. The maximum displacement, \bar{x} , of 256 mm is used as input to the analytical procedure of Section 0 to estimate the frequency, \bar{f} , of the isolated building incorporating the opposing restraints. The $F(x)-x$ relationship drawn as the green solid line in Figure 6b is re-generated in Figure 10a. Given \bar{x} , $F(x)$ is approximated using a 3rd-order polynomial function of x . (The units used for this regression analysis should be consistent with those used for the $F(x)-x$ relationship in Figure 10a, namely, force in MN and displacement in mm.) The regression line is shown as a black dash-dotted line, and the function is noted in the legend: coefficients $c_1 = 8.3 \times 10^{-2}$ MN/mm and $c_3 = 1.2 \times 10^{-6}$ MN/mm³. The black solid circles at the ends of the regression line identify \bar{x} . Given c_1 and c_3 from the regression analysis, $\bar{x} = 256$ mm, and $m = 9 \times 10^{-3}$ megatonnes (consistent with MN and mm), $\bar{\omega} = 4$ rad/sec and $\bar{f} = 0.64$ Hz per Eq. (3).

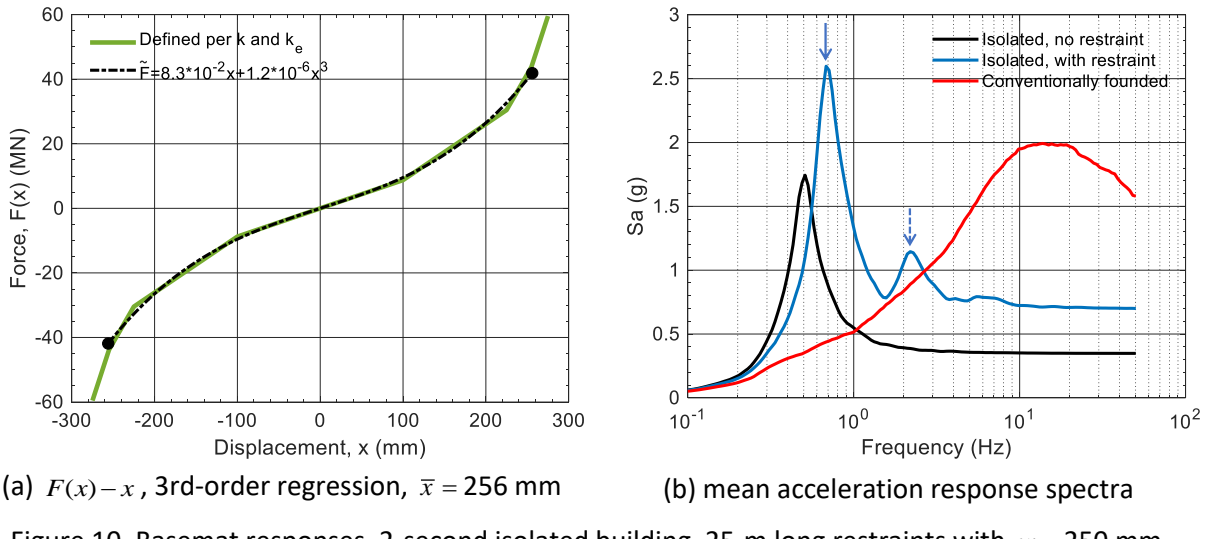


Figure 10. Basemat responses, 2-second isolated building, 25-m long restraints with $w = 250$ mm, $d = 125$ mm, and $e = 100$ mm, 30 matched motions, PGA = 1 g

Figure 10b presents mean acceleration response spectra on the basemat for the 30 inputs for the cases with and without the restraint. The geomean UHRS for the input motions (Figure 7), which represents the response of the non-isolated (or conventionally founded) building, is plotted for reference. For the isolated building, the prominent peak of the mean spectrum is at 0.5 Hz. The first prominent peak in the spectrum for the composite isolation-restraint system is at 0.67 Hz, which is in excellent agreement with the analytical solution of 0.64 Hz. The frequency of the second peak in the spectrum, identified using a blue dashed arrow in Figure 10b, is at 2.1 Hz, which is approximately $3\bar{f}$ ($=3 \times 0.67 = 2.0$ Hz), and consistent with the response of the oscillator per Eq. (4) composed of sinusoids at angular frequencies $\bar{\omega}$ and $3\bar{\omega}$, generated by an initial displacement of \bar{x} . Such outcomes provide a partial verification of the numerical model used for impact analysis and confidence in the computed spectral demands.

Figure 10b presents mean (of 30) acceleration response spectra for three boundary conditions: conventionally founded (not isolated), isolated with no restraint, and isolated with restraint. The spectral demands for both isolation cases (i.e., no restraint, restraint) are smaller than those for the non-isolated building (red line) for frequencies greater than 3 Hz, which is an important outcome for the design of superstructure framing and equipment. For frequencies higher than 1.0 Hz, the spectral demands are smallest for the isolated, no restraint case.

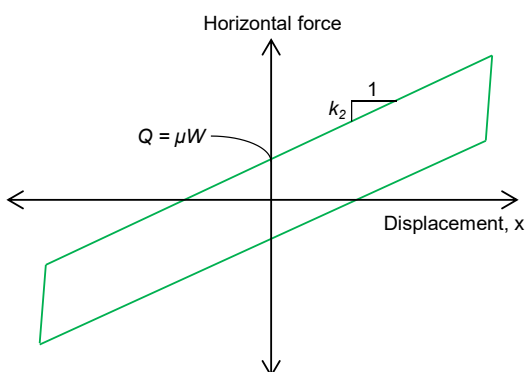
Design solutions for impact of base-isolated buildings

Section 0 presents outcomes associated with adding an engineered displacement restraint to a seismic isolation system, namely, increased spectral accelerations and reduced isolator displacements, wherein the analyst can choose mechanical properties for the restraint to achieve desired system-level responses (e.g., isolation-system displacements limited to abc mm; 5%-damped spectral accelerations limited to xyz g). Commercial finite element software (e.g., SAP 2000¹³ and LS-DYNA¹²) can be used for simulations involving engineered displacement restraints, and neither contact algorithms nor Hertz-type elements, both of which require calibration to test data that do not exist for the scale of the problem defined by Figure 1, are needed.

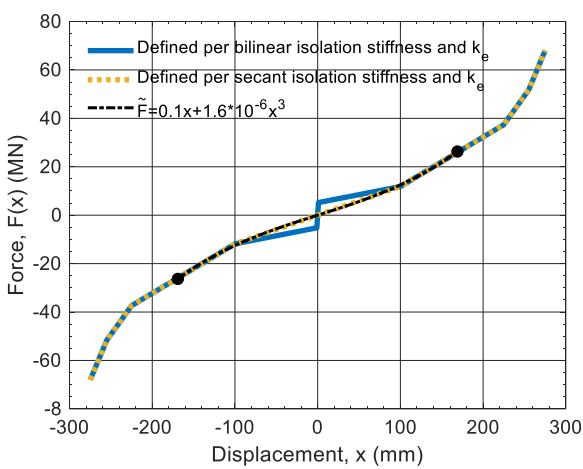
Linear isolation systems and compliant restraints were addressed in Section 0. The most used isolation systems in the United States (e.g., spherical sliding and lead-rubber bearings) exhibit bilinear force-displacement response. Below, the analytical solution of Section 0 is applied to a bilinear isolation system (Section 0) and results of dynamic analysis for *soft* (Section 0) and *hard* impact are compared (Section 0) to identify the merits of restraint stiffness.

Bilinear isolation systems

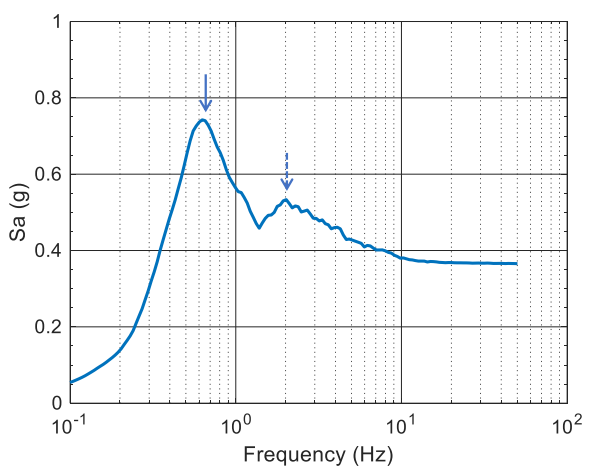
The most widely used 2D isolation systems exhibit the bilinear hysteresis of Figure 11a, which is characterized by a zero-displacement force intercept Q and a second-slope stiffness, k_2 . The analysis of Section 0 is repeated with a bilinear isolation. The period of the bilinear isolation is characterized using its second-slope stiffness: $k_2 = 88 \text{ kN/mm}$. The engineered restraint (marine fender with $w = 250 \text{ mm}$ and $d = 125 \text{ mm}$), and a gap width e of 100 mm are used for the calculations. Figure 11b presents the composite force-displacement, $F(x)-x$, relationship using a blue solid line, for the bilinear isolator-restraint assembly assuming Q equal to 6% of the building weight ($=540 \text{ tonnes}$) at a displacement of 1 mm, resulting in $k_1 = 5300 \text{ kN/mm}$. The composite stiffness associated with the five slopes on either side of the origin is k_1 , k_2 , $k_2 + k_{e1}$, $k_2 + k_{e2}$, and $k_2 + k_{e3}$.



(a) hysteresis of a bilinear isolation



(b) $F(x)-x$, 3rd-order regression, $\bar{x} = 169 \text{ mm}$



(c) mean acceleration response spectrum

Figure 11. Bilinear isolation system with $Q = 540 \text{ tonnes}$ and $k_2 = 88 \text{ kN/mm}$, basemat responses, 25-m long opposing restraints with $w = 250 \text{ mm}$ and $d = 125 \text{ mm}$, $e = 100 \text{ mm}$, 30 matched motions, PGA

$$=1 g$$

The mean maximum displacement, \bar{x} , of the bilinear isolation incorporating the restraints for the 30 inputs, is 169 mm. Figure 11c presents the mean acceleration response spectrum on the basemat. The mean maximum displacement \bar{x} and spectral amplitude are smaller than those for the linear isolation reported in Section 0 (i.e., $\bar{x} = 256$ mm and blue spectrum of Figure 10b) because the bilinear isolation system has much greater equivalent viscous damping (=23%) than the 5% assigned to the linear isolation system. The first prominent peak in the spectrum of Figure 11c is at $\bar{f} = 0.64$ Hz (solid arrow), and the second peak is at 2 Hz (dashed arrow), which is approximately $3\bar{f}$ ($=3 \times 0.64 = 1.9$ Hz).

The analytical procedure of Section 0 is used to calculate \bar{f} to confirm results presented in Figure 11c. The stiffness k of the linear isolation system was replaced by the secant stiffness of the bilinear isolation for $0 \leq x \leq e$: see the yellow dotted line in Figure 11b. The regression line for the yellow $F(x)-x$ relationship is shown as a black dash-dotted line with solid circles at $\pm\bar{x} = 169$ mm, and the function is noted in the legend. Given the regression function and \bar{x} , $\bar{\omega} = 4$ rad/sec and $\bar{f} = 0.63$ Hz per Eq. (3), which is in excellent agreement with the frequency associated with the first spectral peak in Figure 11c. Based on this outcome, the process of Section 0 can be used to verify results of numerical analysis of the two-sided impact of a building equipped with bilinear isolation systems.

Hard impact

The two-sided impact analysis of a linear isolation presented in Section 0 is repeated with hard restraints replacing the compliant engineered restraint. Hard restraints, numbered 1 and 2, with linear stiffness of $10k_{e3}$ ($=7,000$ kN/mm) and $100k_{e3}$ ($=70,000$ kN/mm), respectively, are considered to characterize the effect of substantially increased restraint stiffness on basemat response. (In the absence of a compliant restraint, a range of values for the lateral stiffness of the moat wall-soil assembly would have been considered for calculations.) The damping ratio for the restraint is assumed to be 5%, identical to that of the engineered restraint. (Five percent damping was assigned to the compliant restraint of Section 0 based on stiffness k_{e1} , resulting in much smaller damping at the higher stiffness k_{e3} .) For hard restraint 1 (2), the stiffness k_e and damping coefficient c_e are 7,000 kN/mm and 25 kN-s/mm (70,000 kN/mm and 79 kN-s/mm), respectively. The gap between the basemat and the hard restraints (e.g., moat wall) is 100 mm per Section 0.

Figure 12a and b present the force-displacement relationships for the composite isolation system-hard restraint and mean acceleration response spectra for the 30 inputs, respectively. Companion data for the engineered restraint of Section 0 are included for reference. The mean maximum displacement, \bar{x} , for the models adopting hard restraints 1 and 2, is 126 and 108 mm, respectively. (For the cases of no restraint and the compliant engineered restraint, $\bar{x} = 345$ and 256 mm, respectively, noting that the displacement of 256 mm would be reduced if stiffness-independent damping of 5% had been implemented.) Significant reductions in isolation-system displacement are realized with the hard restraints.

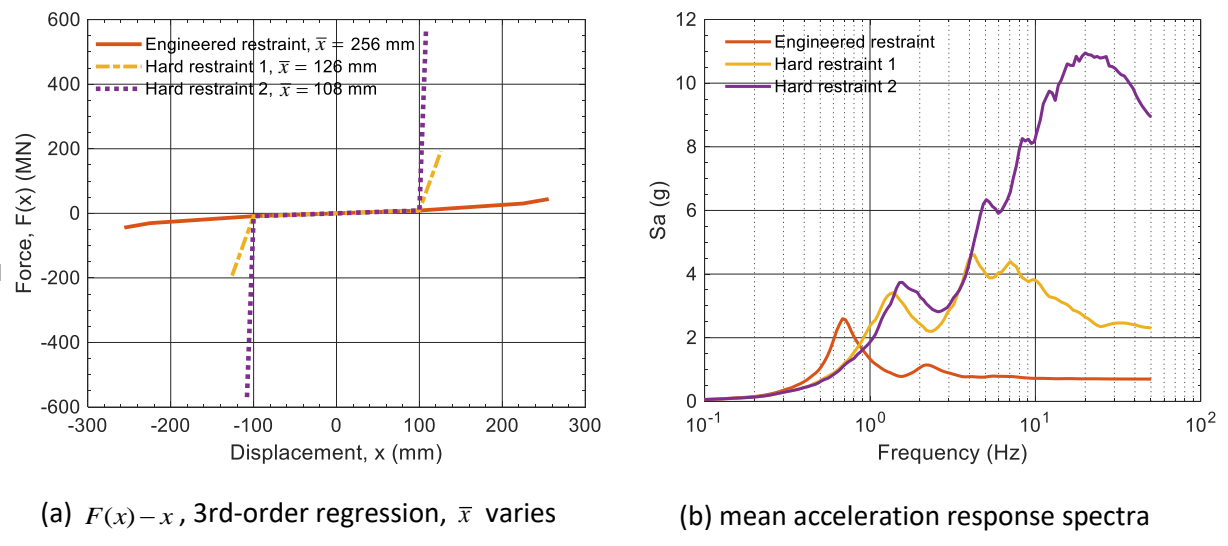


Figure 12. Basemat responses, 2-second isolated building, 25-m long opposing restraints, $e = 100$ mm, 30 matched motions, PGA = 1 g

Third-order polynomials were generated by regression analysis for the $F(x) - x$ relationships of Figure 12a for hard restraints 1 and 2, and $\bar{x} = 126$ and 108 mm, respectively. The corresponding frequencies, \bar{f} , per Eq. (3), are 1.5 and 1.8 Hz.

Figure 12b presents mean acceleration response spectra on the basemat for hard restraints 1 and 2. From the dynamic analysis, the frequencies associated with the first spectral peaks for hard restraints 1 and 2 are 1.4 Hz and 1.9 Hz, respectively, which are in good agreement with the analytical solutions of 1.5 Hz and 1.8 Hz. The three subsequent peaks in the hard restraint 1 (yellow) and 2 (purple) spectra are at (4.3, 7.1, 9.8) Hz and (5.1, 8.3, 12.1) Hz, which are approximately 3, 5, and 7 times the corresponding values of \bar{f} .

One conclusion that can be drawn from analysis of Figure 12b is that the stiffer the displacement restraint, the greater the number of local peaks in the response spectrum, the higher the amplitude of the peak spectral acceleration, and the broader the frequency range of *high* spectral accelerations: compare the red, yellow, and purple plots in Figure 12b.

For the frequency range of interest for both building and equipment design, namely, 1 Hz and higher, the use of a compliant, engineered restraint is a better alternative than a hard restraint, assuming a) a restraint is engaged, and b) the isolation system can accommodate the greater displacement associated with the soft restraint. Per Figure 12b, responses of the isolated building and internal equipment could be substantially excited by hard impact: 0.8 g, 4 g, and 8 g at 10 Hz for the engineered restraint, hard restraint 1, and hard restraint 2, respectively.

Closing remarks

Impact between a seismically base-isolated building and a perimeter moat wall (or surrounding structure) has been investigated via small-scale experiments and numerical analysis in prior studies. Impact has been numerically simulated using contact formulations or springs and dashpots, both of which are challenged by the lack of data at a scale appropriate to the problem addressed in this

paper. Although there is no consensus on how the stiffness and damping ratio for the moat wall should be determined, prior studies have consistently observed that hard impact results in high-frequency, high-amplitude response of the isolated building.

A compliant displacement restraint is an engineered design solution to mitigate the damaging effects of hard impact. Adding a flexible engineered element in the load path makes the stiffness of the restraint-wall assembly insensitive to the highly uncertain lateral stiffness of the wall-soil assembly, eliminating the need for bounding analysis. Simple numerical models for the engineered restraint, with mechanical properties based on physical testing, can be implemented in commercial finite element codes used nowadays to analyze seismically isolated buildings. The results of analysis can be verified using the theory of Section 0. The geometry and mechanical properties of the engineered restraint should be chosen to achieve designer-selected performance objectives, balancing isolation-system displacements and building spectral accelerations, in the event of extreme earthquake shaking.

Acknowledgments

The information, data, and work presented herein was funded in part by the U.S. Department of Energy, under Award Number DE-NE0008932, supporting the first two authors. The authors thank Benjamin M. Carmichael and Jason P. Redd of Southern Company, Mark W. Peres of Peres Engineering LLC, Brian I. Song of Kairos Power, Dr. Chandrakanth Bolisetti of the Idaho National Laboratory, and Dan Murphy of the ShibataFenderTeam for their contributions to this study. The views and opinions of the authors expressed herein do not necessarily state or reflect those of the United States Government, the Idaho National Laboratory, Southern Company, Kairos Power, or the ShibataFenderTeam.

References

1. Kammerer A.M., Whittaker A.S., Constantinou M.C. *Technical considerations for seismic isolation of nuclear facilities*. NUREG/CR-7253. Washington D.C.: Nuclear Regulatory Commission (NRC); 2019.
2. Matsagar V.A., Jangid R. Seismic response of base-isolated structures during impact with adjacent structures. *Engineering Structures*. 2003;25(10):1311-1323.
3. Masroor A., Mosqueda G. Impact model for simulation of base isolated buildings impacting flexible moat walls. *Earthquake Engineering and Structural Dynamics*. 2013;42(3):357-376.
4. Sarebanha A., Mosqueda G., Kim M.K., Kim J.H. Seismic response of base isolated nuclear power plants considering impact to moat walls. *Nuclear Engineering and Design*. 2018;328:58-72.
5. Du H., Wang Y., Han M., Ibarra L.F. Experimental seismic performance of a base-isolated building with displacement limiters. *Engineering Structures*. 2021;244:112811.
6. American Society of Civil Engineers (ASCE). *Minimum design loads and associated criteria for buildings and other structures*. ASCE/SEI 7-22. ASCE, Reston, VA: 2022.
7. Yu C.-C., Carmichael B.M., Redd J.P., et al. Achieving a seismic risk target for a seismically isolated advanced reactor. Paper presented at: 2022 American Nuclear Society (ANS) Winter Meeting; 2022; Phoenix, AZ.
8. Wolf J., Skrikerud P. Mutual pounding of adjacent structures during earthquakes. *Nuclear Engineering and Design*. 1980;57(2):253-275.
9. Timoshenko S. Art 25: Method of successive approximations applied to free vibrations. In: *Vibration problems in engineering*. 2nd ed. New York, NY: D. Van Nostrand Company, Inc.; 1937.
10. Timoshenko S.P., Young D.H., Weaver Jr. W. Section 2.3: Approximate methods for free vibration. In: *Vibration problems in engineering*. 4th ed. Hoboken, NJ: John Wiley & Sons, Inc.; 1974.
11. ShibataFenderTeam Inc. *Extruded fenders*. Accessed May, 2022. <<https://www.shibata-fender.team/en/products/extruded-fenders.html>>

12. Livermore Software Technology Corporation (LSTC). *LS-DYNA keyword user's manual-R11*. Livermore, CA: LSTC; 2018.
13. Computers and Structures (CSI). *SAP2000 Version 22.1.0*. Walnut Creek, CA.: CSI; 2020.
14. United States Geological Survey (USGS). *Hazard curves for the 2018 update of the U.S. National Seismic Hazard Model*. Accessed Feb, 2021.
[<https://www.sciencebase.gov/catalog/item/5d559795e4b01d82ce8e3fef>](https://www.sciencebase.gov/catalog/item/5d559795e4b01d82ce8e3fef)
15. Hancock J., Watson-Lamprey J., Abrahamson N.A., et al. An improved method of matching response spectra of recorded earthquake ground motion using wavelets. *Journal of Earthquake Engineering*. 2006;10(spec01):67-89.
16. Goldsmith W. *Impact: the theory and physical behavior of colliding solids*. 1st ed. Bungay, UK: Richard Clay and Company, Ltd.; 1960.
17. Anagnostopoulos S.A. Equivalent viscous damping for modeling inelastic impacts in earthquake pounding problems. *Earthquake Engineering and Structural Dynamics*. 2004;33(8):897-902.
18. Komodromos P., Polycarpou P.C., Papaloizou L., Phocas M.C. Response of seismically isolated buildings considering poundings. *Earthquake Engineering and Structural Dynamics*. 2007;36(12):1605-1622.
19. Hunt K.H., Crossley F.R.E. Coefficient of restitution interpreted as damping in vibroimpact. *Journal of Applied Mechanics*. 1975;42(5):440-445.
20. Lankarani H.M., Nikravesh P.E. A contact force model with hysteresis damping for impact analysis of multibody systems. *Journal of Mechanical Design*. 1990;112(3):369-376.
21. Ye K., Li L., Zhu H. A note on the Hertz contact model with nonlinear damping for pounding simulation. *Earthquake Engineering and Structural Dynamics*. 2009;38(9):1135-1142.
22. Jankowski R. Non-linear viscoelastic modelling of earthquake-induced structural pounding. *Earthquake Engineering and Structural Dynamics*. 2005;34(6):595-611.
23. Polycarpou P.C., Komodromos P., Polycarpou A.C. A nonlinear impact model for simulating the use of rubber shock absorbers for mitigating the effects of structural pounding during earthquakes. *Earthquake Engineering and Structural Dynamics*. 2013;42(1):81-100.
24. Muthukumar S., DesRoches R. A Hertz contact model with non-linear damping for pounding simulation. *Earthquake Engineering and Structural Dynamics*. 2006;35(7):811-828.
25. Jankowski R. Analytical expression between the impact damping ratio and the coefficient of restitution in the non-linear viscoelastic model of structural pounding. *Earthquake Engineering and Structural Dynamics*. 2006;35(4):517-524.
26. Malhotra P.K. Dynamics of seismic impacts in base-isolated buildings. *Earthquake Engineering and Structural Dynamics*. 1997;26(8):797-813.
27. Komodromos P. Simulation of the earthquake-induced pounding of seismically isolated buildings. *Computers and Structures*. 2008;86(7-8):618-626.
28. Pant D.R., Wijeyewickrema A.C. Structural performance of a base-isolated reinforced concrete building subjected to seismic pounding. *Earthquake Engineering and Structural Dynamics*. 2012;41(12):1709-1716.
29. Hughes P.J., Mosqueda G. Evaluation of uniaxial contact models for moat wall pounding simulations. *Earthquake Engineering and Structural Dynamics*. 2020;49(12):1197-1215.
30. Masroor A., Mosqueda G. Experimental simulation of base-isolated buildings pounding against moat wall and effects on superstructure response. *Earthquake Engineering and Structural Dynamics*. 2012;41(14):2093-2109.
31. Masroor A., Mosqueda G. *Seismic response of base isolated buildings considering pounding to moat walls*. MCEER-13-0003. Buffalo, NY: University at Buffalo; 2013.
32. US Nuclear Regulatory Commission (USNRC). *Design response spectra for seismic design of nuclear power plants (revision 1)*. RG 1.60. Rockville, MD: USNRC; 1973.

Appendix A: Literature review of impact analysis

A.1 Introduction

Studies on impact of base-isolated buildings have identified high-frequency, high-amplitude responses as an outcome. The use of engineered displacement restraints is evaluated in this paper as a *solution* to address earthquake-induced impact between a base-isolated building and surrounding structure, assumed herein to be a moat wall, as shown in Figure 1. This paper is a departure from prior work, and so a literature review of impact models and analysis is presented in this appendix, and not in the body of the paper.

Impact between the basemat and moat wall of Figure 1 has been simulated using contact formulations and spring-dashpot models. If contact formulations (e.g., the *CONTACT card in LS-DYNA¹²) are used, the constraint between the impacting surfaces can be optimized using algorithms, such as the penalty method. Such algorithms generally require modeling at least one of the contact surfaces using shell elements. The algorithm achieves the constraint by adding a series of springs of zero length at the nodes of the contact surface, and the stiffness is optimized at each time step of the analysis, based on the material properties, geometries, response on the surface, and time interval.

Impact elements using spring-dashpot models are attached to one of the two colliding bodies; the elements are compressed upon contact. Impact elements have been used to address one or more of the three *impact mechanisms* identified in Goldsmith (1960)¹⁶: a) stereo-mechanical, b) local-deformation, and c) vibrational. The stereo-mechanical mechanism models the impacting bodies as lumped masses, and their motions are computed using conservation of momentum and a coefficient of restitution. The local-deformation (indentation) mechanism is employed if the impact force on the contact surface is not uniform; examples are a dent on an initially flat surface or a flattened, initially curved surface. Linear or nonlinear springs and dashpots have been used to model the stereo-mechanical and local-deformation mechanisms. The vibrational mechanism addresses the modal properties and dynamic responses of the colliding bodies, which are affected by impact. Chapters II, IV, and III of Goldsmith¹⁶ describe the stereo-mechanical, local-deformation, and vibrational mechanisms, respectively, in detail.

This appendix is focused on the second numerical pathway: impact elements. Section A.2 reviews available models for elements used for *general* impact analysis. Section A.3 reviews studies on analysis of base-isolated buildings with the consideration of the impact mechanisms and the use of the models introduced in Section A.2. Section A.4 presents closing remarks.

A.2 Impact models

Impact models address the relationship between the contact force, F_{ind} , and local indentation (or penetration), δ , between two colliding bodies. Impact models are classed as either linear or nonlinear viscoelastic.

Linear viscoelastic models are described using a constant stiffness and damping coefficient, namely, the Kelvin-Voigt model shown in Figure A-1a. Given a linear stiffness k_A , Anagnostopoulos (2004)¹⁷ derived an analytical solution for the damping coefficient, c_A , used for the Kelvin-Voigt model for impact between two lumped masses, m_1 and m_2 . The derivation accommodated the stereo-

mechanical mechanism: conservation of momentum for m_1 and m_2 . The loss in the kinetic energy of the two moving masses was addressed using the coefficient of restitution, r . A relationship between the damping ratio ξ and r was proposed. The analytical solutions provided c_A and ξ are:

$$c_A = 2\xi \sqrt{k_A \frac{m_1 m_2}{m_1 + m_2}} \quad (\text{A-1})$$

$$\xi = \frac{-\ln(r)}{\sqrt{\pi^2 + (\ln(r))^2}} \quad (\text{A-2})$$

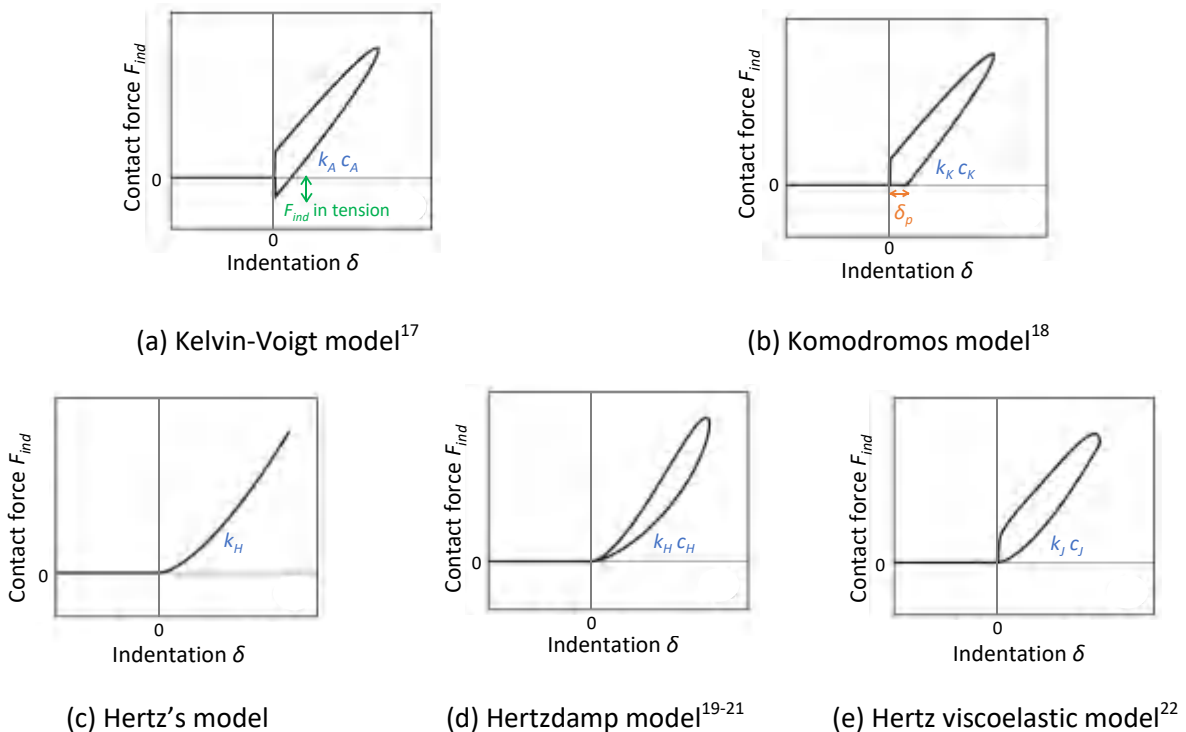


Figure A-1. Impact models, relationship between the contact force, F_{ind} , and indentation, δ , in compression, stiffnesses and damping coefficients identified, modified from Polycarpou et al. (2013)²³

A physical interpretation for k_A was not provided by Anagnostopoulos. Komodromos et al. (2007)¹⁸ developed a F_{ind} - δ relationship by truncating the Kelvin-Voigt model of Figure A-1a along the horizontal axis to eliminate tensile force: see the green notation. This modified Kelvin-Voigt model is described here as the Komodromos model and is plotted in Figure A-1b. The displacement δ_p at $F_{ind} = 0$ is the permanent indentation (or penetration) due to impact: see the orange notation.

The stiffness and damping coefficient used for the nonlinear viscoelastic model are functions of δ . The spring force (stiffness) accommodates the Hertz contact law first proposed in 1881. As reported in Goldsmith¹⁶, the Hertz contact law addresses the F_{ind} - δ relationship for different curved surfaces: $F_{ind} = k_H \cdot \delta^{1.5}$, where k_H is the nonlinear stiffness. Figure A-1c presents the Hertz F_{ind} - δ relationship. Analytical solutions for k_H for contact between two curved surfaces (e.g., spheres and

cylinders) and between a curved surface and a plane are documented in Goldsmith¹⁶. For two spheres, k_H is a function of their radii and material properties:

$$k_H = \frac{4}{3\pi} \left(\frac{1}{\lambda_1 + \lambda_2} \right) \sqrt{\frac{R_1 R_2}{R_1 + R_2}} \quad (\text{A-3})$$

$$\lambda_i = \frac{1 - \nu_i^2}{\pi E_i} \quad (\text{A-4})$$

where the subscripts $i = 1$ and 2 refer to spheres 1 and 2 ; R_i , E_i , and ν_i are the radius, elastic modulus, and Poisson's ratio, respectively, of sphere i . Between a sphere and a plane, k_H is:

$$k_H = \frac{4}{3\pi} \left(\frac{1}{\lambda_1 + \lambda_2} \right) \sqrt{R_1} \quad (\text{A-5})$$

where λ_i is defined in Eq. (A-4), $i = 1$ and 2 refer to the sphere and the plane, respectively, and R_1 is the radius of the sphere. Hunt and Crossley (1975)¹⁹, Lankarani and Nikravesh (1990)²⁰, Jankowski (2005)²², and Ye et al. (2009)²¹ added damping to the Hertz model of Figure A-1c and derived equations for coefficients to address energy loss due to impact. The damping coefficients, c_H , derived by Hunt and Crossley, Lankarani and Nikravesh, and Ye, et al.¹⁹⁻²¹ take the form of:

$$c_H = \xi \delta^{1.5} \quad (\text{A-6})$$

where ξ is a function of r (see the original articles for details). The F_{imp} - δ relationship described using k_H and c_H is named the Hertzdamp model²⁴ and presented in Figure A-1d. The Hertz viscoelastic model²² shown in Figure A-1e follows the form of the Hertz contact law, namely, $F_{ind} = k_J \cdot \delta^{1.5}$, but where k_J is the nonlinear stiffness and replaces k_H . The damping coefficient, c_J , is defined using Eq. (A-1) for the linear viscoelastic model, where k_A is replaced by an equivalent linear stiffness $k_J \sqrt{\delta}$, although no physical basis was presented for doing so. Jankowski²² determined values for k_J and ξ using data from small-scale tests. Based on c_J per Eq. (A-1) with equivalent linear stiffness $k_J \sqrt{\delta}$, Jankowski²⁵ derived analytical solutions for ξ as a function of r , for two impacting masses. The analytical solutions were compared with results from numerical analysis.

A.3 Studies on impact analysis of base-isolated buildings

This section summarizes studies on base-isolated buildings subjected to earthquake-induced impact with a focus on the how impact was modeled. Details of the isolation systems, buildings, adjacent structures, horizontal clearances around the building, ground motions, and analysis results can be found in the cited articles. All the studies summarized below used unidirectional horizontal seismic inputs.

Malhotra (1997)²⁶ analyzed the one-time impact of an isolated building on a moat wall using the stereo-mechanical mechanism introduced above: conserving momentum to calculate velocities after impact. He addressed the post-impact vibration of the isolated building by modal analysis.

A number of studies have sought to calculate the impact force on a building basemat using the F_{ind} - δ models of Figure A-1, and six studies are introduced here. Komodromos et al. (2007)¹⁸, Komodromos (2008)²⁷, and Pant and Wijeyewickrema (2012)²⁸ assumed the impact force was solely generated by the local-deformation mechanism per the F_{ind} - δ models: penetration of the basemat into the moat wall. The moat wall was not physically modeled in these studies. Masroor and

Mosqueda (2013)³, Sarebanha et al. (2018)⁴, and Hughes and Mosqueda (2020)²⁹ calculated the impact force on the basemat considering both local penetration per the F_{ind} - δ models and the modal response of the moat wall: vibrational mechanism. The moat wall was modeled explicitly.

Komodromos, et al.¹⁸ and Komodromos²⁷ used the Kelvin-Voigt model, Komodromos model, and Hertz viscoelastic model shown in Figures A-1a, b, and e, respectively, for impact analysis of an isolated building. The building was modeled using lumped masses and beam-column elements. The stiffnesses, k_A , k_K , and k_J , used in the impact models were calibrated using an impact-force time series, generated by a separate nonlinear finite element analysis of a concrete basemat colliding one time at an assumed velocity. The damping coefficients c_A , c_K , and c_J were calculated using Eq. (A-1) for a coefficient of restitution $r=0.7$. The penetration, δ_p , calculated from the finite element analysis and that considered in the F_{ind} - δ model of Figure A-1b were not compared. The differences in the responses (i.e., displacements and accelerations on the floors and the story drifts) calculated using the three F_{ind} - δ models were insignificant (<10%). Pant and Wijeyewickrema²⁸ used the Komodromos model shown in Figure A-1b to simulate impact between a base-isolated building and rigid retaining wall(s), on one or two sides of the building. The building was modeled using beam-column elements and rigid diaphragms for the floor slabs. The stiffness k_K for the F_{ind} - δ model of Figure A-1b was assumed to be identical to the axial (in-plane) stiffness of the impacting slab: the impact was assumed to deform (shorten) the slab but not the moat wall. The damping coefficient, c_K , was determined using Eq. (A-1) for $r=0.65$. Given identical seismic inputs and clearances, the authors observed that story drifts were greater for one-sided impact.

Masroor and Mosqueda³ studied the impact of a 1/4-length-scale, base-isolated steel frame on opposing moat walls of the same construction. Pairs of steel and concrete-soil moat walls were used for testing to investigate the influence of moat-wall stiffness and damping on impact response. Analysis results were compared with data from earthquake-simulator experiments for unidirectional horizontal inputs^{30, 31}. Concrete blocks were installed outboard of the base of the steel frame to impact the moat walls. A load cell was placed behind each concrete block to measure impact forces. Details of the test setup can be found in Masroor and Mosqueda^{30, 31}.

For analysis, the steel frame was modeled using elastic beam-column elements and nonlinear rotational springs. Each moat wall was modeled as a single-degree-of-freedom oscillator with a first modal mass and stiffness derived using analytical calculations. The damping ratio used for the moat-wall oscillator was calibrated using test data: 40% of critical for the steel walls and between 160% and 200% of critical for the concrete walls. A Hertzdamp model of Figure A-1d was attached to the moat-wall oscillator to simulate local penetration. A stiffness k_H per Eq. (A-5) was used for the Hertzdamp model, wherein the concrete block and moat wall were assumed to be a sphere and a plane, respectively. The radius R_l in Eq. (A-5) was determined by equating the volumes of the concrete block to a sphere of the same material. The damping coefficient c_H was calculated per Eq. (A-6) with ξ based on $r=0.7$ ²¹. The numerical model reasonably simulated the impact force and seismic responses of the superstructure, including displacements, velocities, accelerations, and story drifts, but it is unclear how some of the assumptions (e.g., treating the impacting cuboid concrete block as an equivalent sphere) could be applied to isolated buildings and infrastructure.

Hughes and Mosqueda²⁹ extended the analysis of Masroor and Mosqueda³ to use all five F_{ind} - δ models shown in Figure A-1 for the impact element. For Figures A-1c, d, and e, the nonlinear stiffness was assumed to be k_H per Eq. (A-5), equating the volumes of the concrete block and the sphere. For the models of Figures A-1a and b, the linear stiffness was computed as $k_H \sqrt{\delta_m}$, where δ_m was the assumed maximum penetration of the basemat into the moat wall. The damping coefficient was calculated using ξ based on $r=0.7$ per Eq. (A-1) for the models of Figures A-1a, b, and e, and per Eq. (A-6) for the model of Figure A-1d. The response of the frame was not affected by the choice of the F_{ind} - δ models as expected because all 5 impact models are based on k_H per Eq. (A-5), and the response of the steel frame was dominated by the properties of the moat-wall oscillator and not the impact element. Per the article, the impact element at $\delta = \delta_m$ was one to two orders of magnitude stiffer than the moat-wall oscillator.

Sarebanha, et al.⁴ investigated the earthquake-induced impact between a base-isolated nuclear power plant (NPP) and a moat wall due to earthquake shaking. The NPP was modeled with beam-column elements, springs, and lumped masses. The moat wall was modeled using lumped masses, elastic beam-column elements, and nonlinear rotational springs at the base and adjacent to the expected point of impact. Impact elements, accommodating the Hertzdamper model of Figure A-1d, were attached to one side of the moat wall, and horizontal springs and dashpots were attached to the other side to simulate supporting soil. The stiffness, k_H , for the Hertzdamper model was calculated per Eq. (A-5): the moat wall and the isolated building, each of unit width, were assumed to be a sphere and a plane, respectively. The value for c_H was calculated per Eq. (A-6) with ξ based on $r=0.8$ ²¹. The authors reported increases in floor spectral accelerations at frequencies greater than 1 Hz, with respect to companion simulations without impact.

A.4 Closing remarks

Figure A-1 introduces impact models available in the literature. All were developed to analyze the one-time collision of objects of simple shapes, and all require calibration using test data. The available test data for colliding objects is small scale.

Prior studies provide insight into earthquake-induced impact: hard impact results in a high-frequency, high-amplitude response of the isolated building. Seven articles^{3, 4, 18, 26-29} in the literature on impact of base-isolated buildings were reviewed. Masroor and Mosqueda³ reported results of small-scale experiments and companion numerical studies. Only numerical simulations were presented in the remaining six papers^{4, 18, 26-29}. All the numerical simulations used impact elements developed previously to address collisions of very simple shapes, and/or assumptions not directly applicable to civil engineering impact problems on the scale of Figure 1. These numerical simulations and impact elements are challenged by the need for validation, calibration to application-specific data, and adapting assumptions from one problem statement (e.g., hard impact) to another. This paper aims to change the problem statement from 1) confirm that hard impact generates significant responses on an isolated building, to 2) develop theory and numerical solutions to mitigate the effects of impact using an engineered restraint.

APPENDIX B: WOLF AND SKRIKERUD (1980)

B.1 Introduction

Wolf and Skrikerud (1980)⁸ modeled buildings using SDF systems for one- and two-sided impact analysis. Closed-form solutions were developed for the modal period and free-vibration response of the SDF models for one-sided impact only. Response spectra were used to quantify the effects of impact. Section 0 of this paper extends the Wolf and Skrikerud article to two-sided impact. To support the derivations presented in Section 0 for two-sided impact, Section B.2 reviews the theory and numerical solutions provided in the Wolf and Skrikerud article. One analytical solution is corrected. Response spectra for a SDF oscillator associated with one-sided impact are computed by analysis using SAP 2000¹³ and compared with spectra digitized from the original article.

B.2 Analytical and numerical solutions

Figures B-1a and b present models of a SDF oscillator for one- and two-sided impact analysis, respectively. The oscillator (building) is defined using a mass, m , a spring with linear stiffness, k , and a viscoelastic dashpot with damping coefficient, c . Impact element(s) are attached to a rigid boundary that moves with the ground and are characterized by a spring with linear stiffness k_e and a dashpot with coefficient c_e . The at-rest clearance between the oscillator and the impact element(s) is e . The ground motion is a displacement input x_g . The oscillator displacement relative to the ground is x . Per Figure B-1, the relationship between the spring force acting on the oscillator, $F(x)$, and displacement x is piecewise linear. The $F(x)$ - x relationship is a function of k , k_e , and e . For two-sided impact, if $|x| \leq e$, $F(x)$ is proportional to k . If $|x| > e$, the increment in $F(x)$ is proportional to $k + k_e$, defined as κk in Figure B-1. For one-sided impact per Figure B-1b, the force $F(x)$ is associated with $k + k_e$ if $x > e$, and k otherwise.

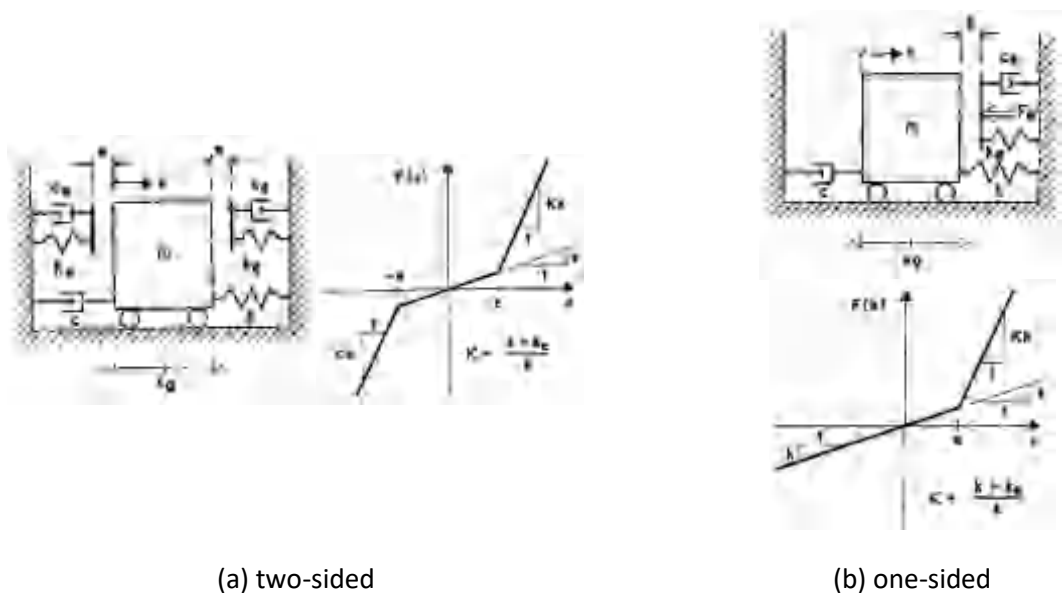


Figure B-1. Oscillators, impact elements, and force-displacement relationships⁸

The period of the oscillator in the absence of impact is $T = 2\pi\sqrt{m/k}$. Wolf and Skrikerud derived analytical solutions for the period and free-vibration response of the impacting oscillator. The effect of damping (i.e., c and c_e) was ignored. The initial condition for the undamped free-vibration response of the oscillator was a positive displacement \bar{x} that was greater than the gap e . The oscillator engaged with the impact element, and the period reduced from T to \bar{T} , depending on k_e and \bar{x} .

For the two-sided impact of Figure B-1a, the analytical solution for oscillator period is:

$$\bar{T} = \frac{2\pi}{\bar{\omega}} = \left(\kappa^{-1/2} \arccos \lambda + \arctan \left(\frac{\kappa \lambda^2}{1 - \lambda^2} \right)^{1/2} \right) \quad (\text{B-1})$$

where $\kappa = (k + k_e)/k$ and $\lambda = [\kappa(\bar{x}/e - 1) + 1]^{-1}$. A solution for the free-vibration response of the oscillator was not provided.

For the one-sided impact of Figure B-1b, the oscillator period is:

$$\bar{T} = \frac{T}{\pi} \left(\kappa^{-1/2} \arccos \lambda - \arctan \left(\frac{\kappa \lambda^2}{1 - \lambda^2} \right)^{-1/2} + \pi \right) \quad (\text{B-2})$$

where κ and λ are defined previously, and \bar{x} , which is used to define λ , is in the $+x$ (impact) direction. The analytical solution for \bar{T} in the original article includes misplaced parentheses and is corrected in Eq. (B-2). For one-sided impact, and the limiting conditions of $k_e = \infty$ and $e = 0$, the period \bar{T} and the free-vibration response x of the oscillator are:

$$\bar{T} = T/2 \quad (\text{B-3})$$

$$x(t) \approx \frac{4}{\pi} \left(\frac{1}{2} - \frac{1}{1.3} \cos \bar{\omega}t - \frac{1}{3.5} \cos 2\bar{\omega}t - \frac{1}{5.7} \cos 3\bar{\omega}t \dots \right) \quad (\text{B-4})$$

where the free-vibration response of the undamped oscillator is an infinite sum of sinusoids with angular frequencies of $\bar{\omega}$ and integer multiples (i.e., 2, 3, 4, 5) of $\bar{\omega}$.

Wolf and Skrikerud reported results of response-history analysis of the SDF oscillator of Figure B-1b for one synthetic ground motion input: a broadband Regulatory Guide 1.60 spectrum³² anchored to a peak ground acceleration of 1 g. The authors presented the acceleration time series in the article, but it could not be digitized. A 10%-damped displacement spectrum was presented for the synthetic motion (Figure 17), which was digitized and replotted as pseudo-acceleration response spectrum in Figure B-3a, together with the 10%-damped RG spectrum. The two spectra are in good agreement for frequencies between 0.1 and 5 Hz.

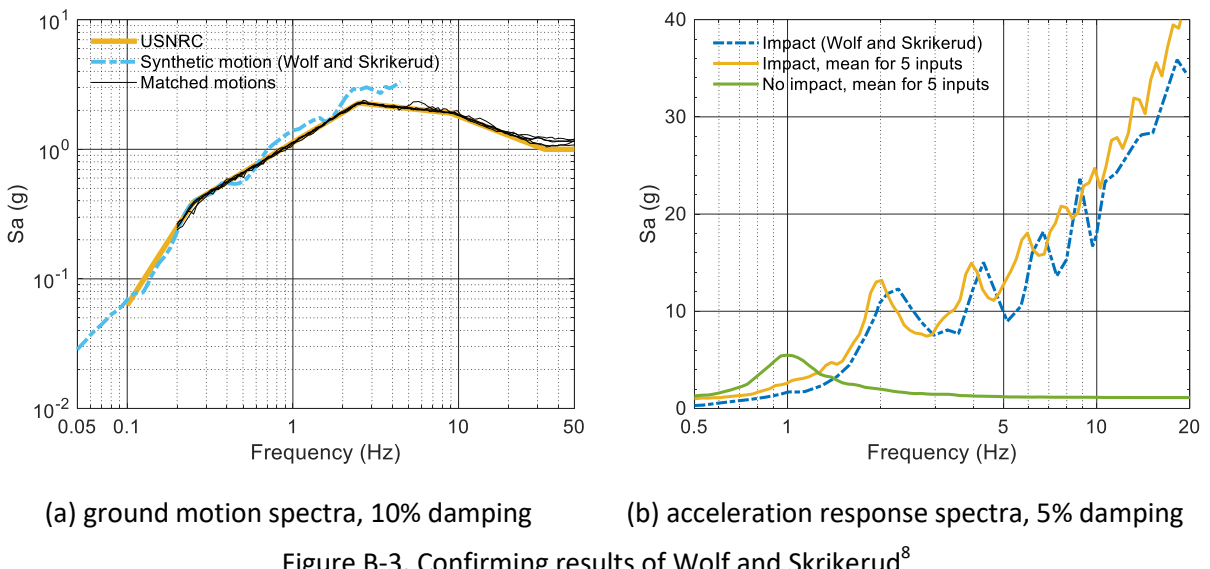


Figure B-3. Confirming results of Wolf and Skrikerud⁸

Figure 20b in Wolf and Skrikerud⁸ presents 5%-damped acceleration response spectra for the one-sided impact of a 10%-damped 1-Hz oscillator for the limiting condition of zero gap (i.e., $e = 0$) and an infinitely stiff restraint (i.e., $k_e = \infty$). (The software used for the calculations is not reported.) This plot was digitized and is presented in Figure B-3b as a blue dash-dotted line. To confirm these results, response-history analysis was performed using five motions that were spectrally matched¹⁵ to the RG 1.60 spectrum: the thin black lines in Figure B-3a. A numerical model was built in SAP 2000¹³ for a 10%-damped 1-Hz oscillator with a nonlinear spring as the impact element: stiffness of k_e in compression and 0 in tension. The linear impact stiffness k_e was set to 2500 times that of the 1-Hz oscillator to be numerically rigid. Since the impact element does not deform, its damping was set to zero (i.e., $c_e = 0$). Results of the SAP 2000 analysis are plotted in Figure B-3b using a yellow solid line. Although the input motions for the Wolf and Skrikerud and the SAP 2000 analyses are different per Figure B-3a, the yellow solid and blue dash-dotted spectra are in reasonable agreement in terms of frequencies at the spectral peaks, amplitudes of the spectral peaks, and trend of increasing spectral acceleration with frequency. The green line in Figure B-3b presents the SAP 2000 acceleration response for the no-impact case: the frequency at the peak spectral response is at 1 Hz, which is the frequency of the oscillator. The peaks in the yellow *impact* spectrum of Figure B-3b are at a frequency $\bar{f} = 2$ Hz ($=1/\bar{T}$ per Eq. (B-3) for an oscillator of $T = 1$ second) and integer multiples of 2 Hz, consistent with the frequencies of the sinusoids per Eq. (B-4).